LETTER

doi:10.1038/nature21042

Deciphering chemical order/disorder and material properties at the single-atom level

Yongsoo Yang[1]*, Chien-Chun Chen[1,2]*, M. C. Scott[1,3]*, Colin Ophus[3]*, Rui Xu[1], Alan Pryor Jr.[1], Li Wu[1], Fan Sun[4], Wolfgang Theis[5], Jihan Zhou[1], Markus Eisenbach[6], Paul R. C. Kent[7,8], Renat F. Sabirianov[9], Hao Zeng[4], Peter Ercius[3] & Jianwei Miao[1]

Perfect crystals are rare in nature. Real materials often contain crystal defects and chemical order/disorder such as grain boundaries, dislocations, interfaces, surface reconstructions and point defects[1–3]. Such disruption in periodicity strongly affects material properties and functionality[1–3]. Despite rapid development of quantitative material characterization methods[1,4–18], correlating three-dimensional (3D) atomic arrangements of chemical order/disorder and crystal defects with material properties remains a challenge. On a parallel front, quantum mechanics calculations such as density functional theory (DFT) have progressed from the modelling of ideal bulk systems to modelling 'real' materials with dopants, dislocations, grain boundaries and interfaces[19,20]; but these calculations rely heavily on average atomic models extracted from crystallography. To improve the predictive power of first-principles calculations, there is a pressing need to use atomic coordinates of real systems beyond average crystallographic measurements. Here we determine the 3D coordinates of 6,569 iron and 16,627 platinum atoms in an iron-platinum nanoparticle, and correlate chemical order/disorder and crystal defects with material properties at the single-atom level. We identify rich structural variety with unprecedented 3D detail including atomic composition, grain boundaries, anti-phase boundaries, anti-site point defects and swap defects. We show that the experimentally measured coordinates and chemical species with 22 picometre precision can be used as direct input for DFT calculations of material properties such as atomic spin and orbital magnetic moments and local magnetocrystalline anisotropy. This work combines 3D atomic structure determination of crystal defects with DFT calculations, which is expected to advance our understanding of structure–property relationships at the fundamental level.

Intermetallic compounds such as FePt with an ordered face-centred tetragonal ($L1_0$) phase are very promising candidates for next-generation magnetic data storage media and permanent magnet applications[21–25]. As-synthesized, FePt thin films and nanoparticles have a chemically disordered face-centred cubic (fcc) structure (A1 phase). When annealed at high temperatures, they undergo a transition from an A1 phase to an $L1_0$ phase or to a chemically ordered fcc ($L1_2$) phase, depending on the chemical composition[22–25]. Owing to the chemical ordering and strong spin–orbit coupling, $L1_0$ FePt exhibits extremely large magnetocrystalline anisotropy energy (MAE)[21]. DFT calculations of model FePt nanoparticles have been performed to elucidate the roles of morphology, capping layers and surface segregation in determining the particles' spin, orbital magnetic moments and MAE[24,26,27], which were compared with experimental measurements from electron microscopy, magnetometry and X-ray magnetic circular dichroism[24,28,29]. However, despite extensive studies of this material system, a fundamental understanding of 3D chemical order/disorder, crystal defects and the resulting magnetic properties at the individual atomic level remains elusive. Here we report the precise determination of the 3D coordinates and chemical species of 23,196 atoms in a single 8.4-nm $Fe_{0.28}Pt_{0.72}$ nanoparticle using atomic electron tomography (AET)[1].

FePt nanoparticles were synthesized and annealed at 600 °C for 25 min to induce partial chemical ordering (Methods). Using an aberration-corrected scanning transmission electron microscope (STEM) operated in annular dark-field (ADF) mode (Extended Data Table 1), we acquired tomographic tilt series from several FePt nanoparticles. A representative tilt series of 68 images with a tilt range from −65.6° to +64.0° was chosen for the detailed analysis because of its structural complexity (Extended Data Fig. 1). After image de-noising and alignment (Methods), a 3D reconstruction was computed from the tilt series using a generalized Fourier iterative reconstruction (GENFIRE) algorithm (Methods). By iterating between real and reciprocal space, GENFIRE searches for a best-possible solution that is concurrently consistent with the measured images and the general physical constraints. GENFIRE can also refine all the tilt angles to improve the 3D reconstruction. Both numerical simulation and experimental results indicate that GENFIRE results in higher resolution and contrast and can tolerate a larger missing wedge than other iterative algorithms (Methods), where the missing wedge is due to the geometric constraint preventing samples from being tilted between ±90°. Supplementary Video 1 shows the 3D reconstruction of the FePt nanoparticle with individual Fe and Pt atoms clearly distinguishable.

From the 3D reconstruction, we developed an atom tracing and classification method to determine the coordinates of all individual Fe and Pt atoms based on their local intensity distribution (Methods, Extended Data Figs 2 and 3). This process resulted in a 3D atomic model of 16,627 Pt and 6,569 Fe atoms. To verify this atomic model, we applied multislice simulations to calculate 68 ADF-STEM images from the model using the same experimental parameters (Method). Extended Data Fig. 4a–c shows good agreement between a measured and a simulated (multislice) image. Using the same reconstruction, atom tracing and classification procedures, we obtained a new 3D model consisting of 16,577 Pt and 6,747 Fe atoms. Compared to the experimental atomic model, 99.0% of all atoms are correctly identified in the new 3D model and the root-mean-square deviation of the common atom positions is 22 pm. (Extended Data Fig. 4d). To further confirm the precision of our atomic position measurements, we performed a lattice and structural analysis of the experimental 3D atomic model and determined the atomic displacements of the nanoparticle (Extended Data Figs 5 and 6).

[1]Department of Physics and Astronomy and California NanoSystems Institute, University of California, Los Angeles, California 90095, USA. [2]Department of Physics, National Sun Yat-sen University, Kaohsiung 80424, Taiwan. [3]National Center for Electron Microscopy, Molecular Foundry, Lawrence Berkeley National Laboratory, Berkeley, California 94720, USA. [4]Department of Physics, University at Buffalo, the State University of New York, Buffalo, New York 14260, USA. [5]Nanoscale Physics Research Laboratory, School of Physics and Astronomy, University of Birmingham, Edgbaston, Birmingham B15 2TT, UK. [6]National Center for Computational Sciences, Oak Ridge National Laboratory, Oak Ridge, Tennessee 37831, USA. [7]Computer Science and Mathematics Division, Oak Ridge National Laboratory, Oak Ridge, Tennessee 37831, USA. [8]Center for Nanophase Materials Sciences, Oak Ridge National Laboratory, Oak Ridge, Tennessee 37831, USA. [9]Department of Physics, University of Nebraska at Omaha, Omaha, Nebraska 68182, USA.
*These authors contributed equally to this work.

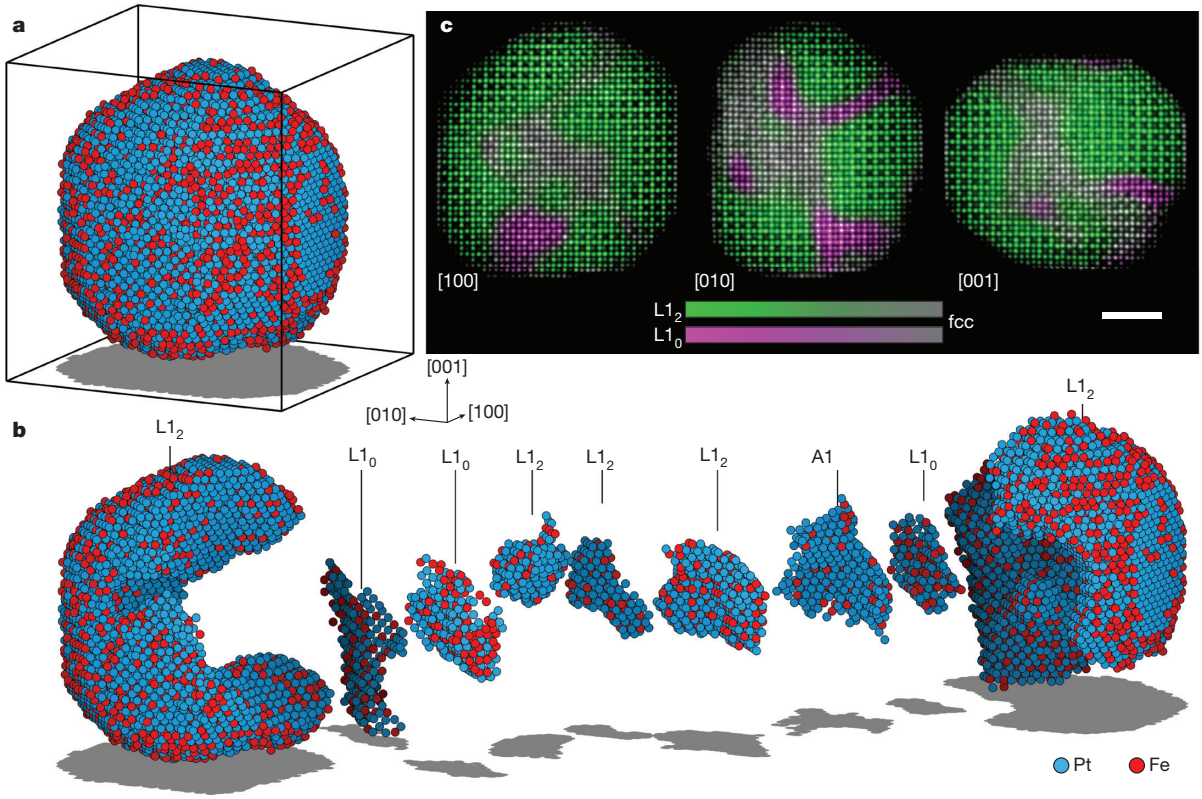

Figure 1 | 3D determination of atomic coordinates, chemical species and grain structure of an FePt nanoparticle. a, Overview of the 3D positions of individual atomic species with Fe atoms in red and Pt atoms in blue. **b**, The nanoparticle consists of two large $L1_2$ grains, three small $L1_2$ grains, three small $L1_0$ grains and a Pt-rich A1 grain. **c**, Multislice images obtained from the experimental 3D atomic model along the [100], [010] and [001] directions, where several '$L1_0$ grains' (magenta) appearing in the 2D images are deceptive structural information. Colour bars indicate the degree of ordering, from pure $L1_2/L1_0$ to chemically disordered fcc. Scale bar, 2 nm.

By comparing the atomic positions to an ideal fcc lattice, we estimated an average 3D precision of 21.6 pm (Extended Data Fig. 7a), which agrees with the multislice result.

Next, we classified the 3D chemical order/disorder of the FePt nanoparticle by determining the short-range order parameter (SROP) of all phases present in the 3D structure (Methods). The nanoparticle consists of two large $L1_2$ $FePt_3$ grains with interlocking concave shapes (Fig. 1). Seven smaller grains are located at the boundary between the two large $L1_2$ grains, including three $L1_2$ $FePt_3$ grains, three $L1_0$ FePt grains and a Pt-rich A1 grain (Fig. 1b and Supplementary Video 2). This level of complexity of the 3D chemical order/disorder can only be fully revealed by AET[1]. To illustrate this point, we used multislice ADF-STEM simulations to calculate 2D images from the 3D atomic model along the [100], [010] and [001] directions (Fig. 1c). Several '$L1_0$ grain' signatures appearing in the 2D images (magenta in Fig. 1c) are actually deceptive structural information, derived from the overlapping of the two large $L1_2$ grains.

Figure 2a shows the 3D grain boundaries (black lines) of the nanoparticle. The grains are more ordered in their cores and become less ordered closer to their surfaces. Four representative cut-outs of the atomic model are shown in Fig. 2b–e. The most chemically ordered region of the nanoparticle is at the core of a large $L1_2$ grain with a SROP close to 1 (Fig. 2b). Figure 2c shows the grain boundary width varying between two large $L1_2$ grains. Anti-phase boundaries between the two $L1_2$ grains are also observed (Extended Data Fig. 7b). The largest $L1_0$ grain is shown in Fig. 1b (third grain from the left) and Fig. 2d. This $L1_0$ grain sits between the two large $L1_2$ $FePt_3$ grains (Fig. 2a) with each of its two Fe sub-lattices matching the Fe sub-lattice of the neighbouring $L1_2$ grains (Extended Data Fig. 5), suggesting the shared Fe lattice with its neighbouring grains may have facilitated the nucleation of the $L1_0$ phase. The central region of the nanoparticle has the highest degree of chemical disorder, including a Pt-rich A1-phase grain (Fig. 2e), with much lower SROP values than those in the two large $L1_2$ grains.

To probe the 3D chemical order/disorder at the single-atom level, we analysed individual anti-site point defects in the 3D reconstruction of the nanoparticle. Figure 3a, b and Extended Data Fig. 7b show 3D atomic positions overlaid on the reconstructed intensity of several representative anti-site point defects (arrows) in the $L1_2$ grains, where an Fe atom occupies a Pt atom site or vice versa. The anti-site point defects in these figures are clearly visible by comparing their local peak intensity with that of the nearby Pt and Fe atoms. Furthermore, swap defects are also observed (Fig. 3c), where a pair of nearest-neighbour Fe and Pt atoms are swapped. Overall, the FePt nanoparticle contains a substantial number of anti-site defects and chemical disorder. Figure 3e and g shows the anti-site defect density of the two large $L1_2$ grains (inset) as a function of the distance from the grain surface. Far outside each grain, the anti-site defect density approaches ~50%, because two of the four sub-lattices in the two large $L1_2$ grains share the same sites of Pt atoms, while the other two sub-lattices swap Fe for Pt atoms and vice versa (Extended Data Fig. 5). The anti-site defect density drops to below 40% at the surface of the two grains and reduces to ~3% for sites deep inside each grain. Figure 3f and h shows the SROP of the two large $L1_2$ grains as a function of the distance from the grain surface.

The striking similarities between the two large $L1_2$ grains—each has a concave shape with a highly-ordered core, a similar chemically disordered boundary and a consistent distribution of the anti-site defect density (Fig. 3e–h)—suggest a potential formation pathway in the nucleation and growth process of the nanoparticle. We note that as-synthesized FePt nanoparticles show large chemical disorder with a Pt-rich core[30]. Such a 3D Pt-rich core is observed in our measurements (Fig. 2e). During the annealing process, Pt atoms diffused out from the core[30] and the nucleation of the $L1_2$

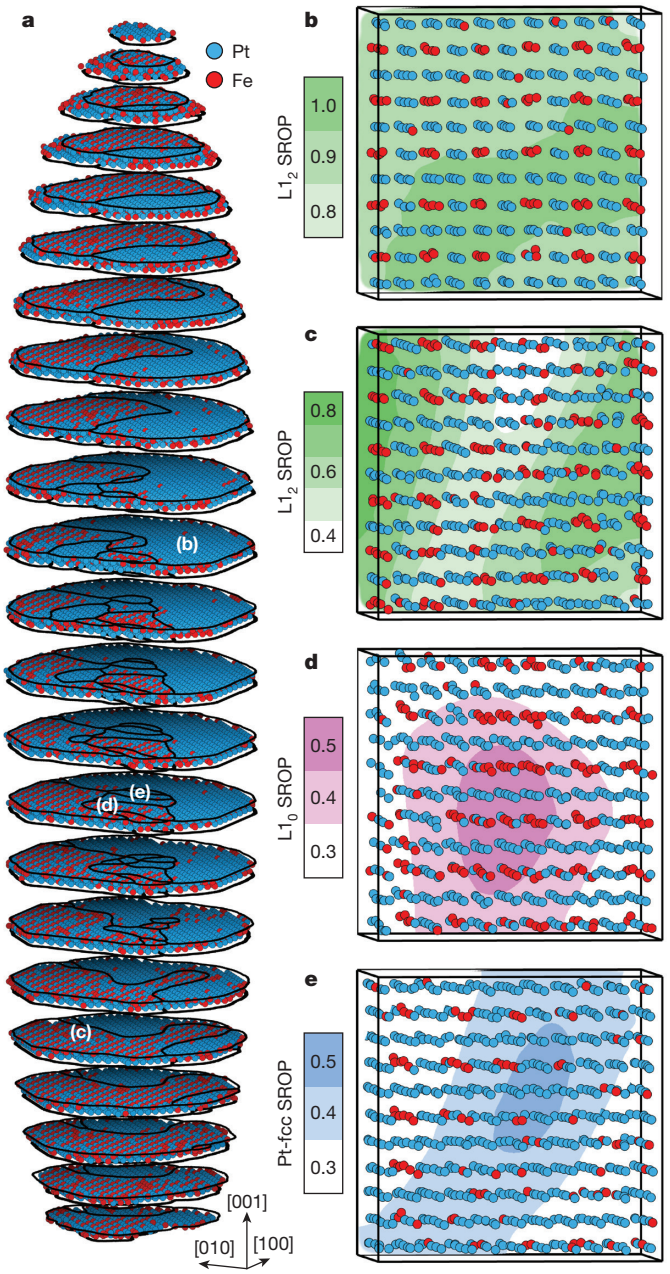

Figure 2 | 3D identification of grain boundaries and chemical order/disorder. a, Atomic coordinates and species of the FePt nanoparticle divided into slices one fcc unit-cell thick. The grain boundaries are marked with black lines. **b**–**e**, Four representative cut-outs of the experimental atomic model, showing the most chemically ordered $L1_2$ region of the particle (**b**), a grain boundary between the two large $L1_2$ grains (**c**), the largest $L1_0$ grain (**d**), and the most chemically disordered region of the particle centred on a Pt-rich A1 grain (**e**). The locations of the cut-outs are labelled in parentheses in **a**, and the SROP of each cut-out is averaged along the [010] viewing direction and displayed as the background colour (see colour bar at left of **b**–**e**).

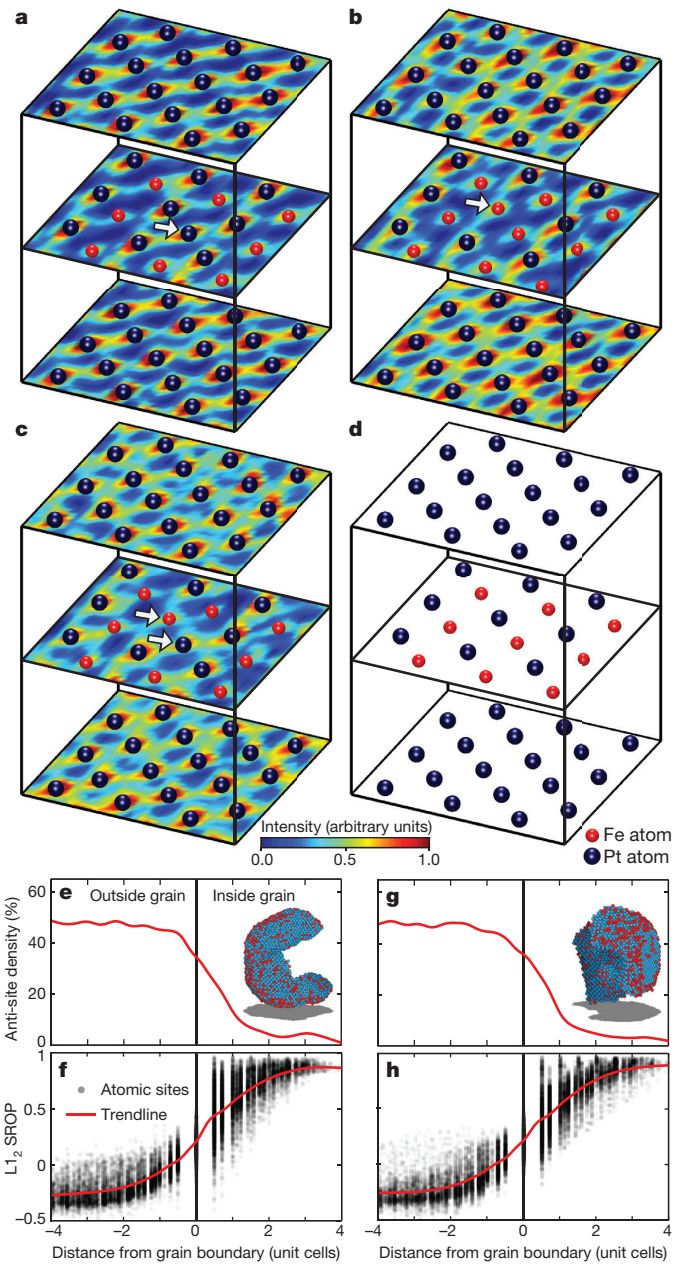

Figure 3 | Observation of anti-site point and swap defects, and statistical analysis of the chemical order/disorder and anti-site density. a–**c**, 3D atomic positions overlaid on the 3D reconstructed intensity (colour scale at bottom) illustrating anti-site point defects (arrows): a Pt atom occupying an Fe atom site (**a**), an Fe atom occupying a Pt atom site (**b**), a pair of nearest-neighbour Fe and Pt atoms are swapped (swap defect) (**c**). **d**, 3D atomic structure of an ideal $L1_2$ $FePt_3$ phase for reference. The anti-site defect density (**e**) and SROP (**f**) for a large $L1_2$ grain, inset in (**e**), as a function of the distance from the grain surface (unit cell size = 3.875 Å). The anti-site defect density (**g**) and SROP (**h**) for the other large $L1_2$ grain, inset in (**g**), as a function of the distance from the grain surface. Smooth red trend lines are overlaid on the defect density distribution as a guide for the eye.

phase occurred at multiple sites in the nanoparticle. The nuclei then grew and merged into larger grains by the Ostwald ripening process[31]. This process would continue until the nanoparticle became a single crystal if sufficiently high temperature or long time annealing was applied. However, if the annealing process was stopped at some intermediate stage, two or more larger grains with similar sizes could coexist, as it would be difficult for either to annihilate the others. The chemical ordering at the grain boundaries would then be frustrated by competition between neighbouring grains. However, determining the particle's chemical structure growth pathway with certainty will require adding the dimension of time to the AET measurements[1].

To correlate measured atomic coordinates and chemical order/disorder with magnetic properties, we performed DFT calculations of the atomic magnetic moments and MAEs. We focused on one of the grain boundaries between two large $L1_2$ grains, where the largest $L1_0$ grain is located, and computed the MAE of different local regions using two independent methods, namely, full supercell and sliding

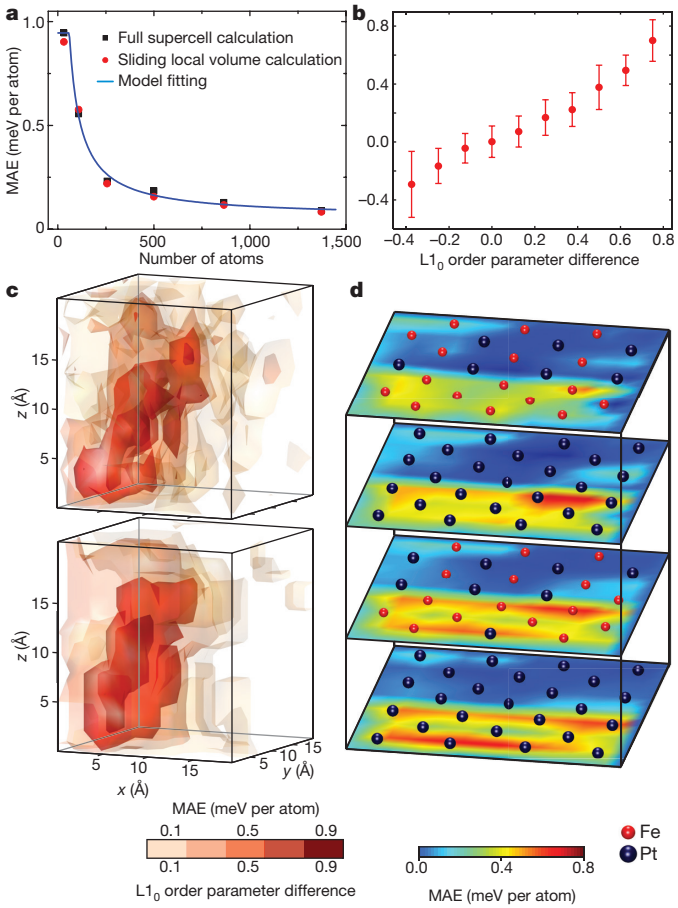

Figure 4 | Local MAEs between the [100] and [001] directions determined using measured atomic coordinates and species as direct input to DFT. a, Black squares represent the MAEs calculated from six nested cubic volumes of 32, 108, 256, 500, 864 and 1,372 atoms ('full supercell calculation'). The blue curve shows the results of fitting a $L1_0$ sphere inside cubic $L1_2$ grains with different sizes. Red dots are the local MAEs averaged by sliding a 32-atom volume inside the corresponding six supercells. **b**, MAEs of all sliding 32-atom volumes inside a 1,470-atom supercell as a function of the $L1_0$ order parameter difference. The $L1_0$ order parameter difference was obtained by subtracting the SROP along the [100] direction from that along the [001] direction and the SROP was computed from each 32-atom volume. Dots and error bars represent the mean and standard deviation, with the number of 32-atom volumes $n = 2$, 17, 63, 631, 284, 164, 92, 128, 45 and 26 (from left to right). The negative MAE values indicate that their local magnetic easy axis is along the [100] instead of the [001] direction. **c**, 3D iso-surface rendering of the local MAE (top) and $L1_0$ order parameter differences (bottom) inside the 1,470-atom supercell. **d**, Local MAE distribution at an $L1_0$ and $L1_2$ grain boundary, interpolated from the sliding local volume calculations and overlaid with measured atomic positions.

local volume calculations (Methods). Figure 4a and Extended Data Fig. 8a show a good agreement of the MAE calculated by these two methods. The MAE decreases with the increase of the number of atoms because the main contribution to the MAE comes from the embedded $L1_0$ grain. Figure 4b and Extended Data Fig. 8b show a strong correlation between the local MAEs inside a 1,470-atom supercell and the $L1_0$ order parameter difference. The 3D distribution of the local MAEs matches well with that of the $L1_0$ order parameter difference (Fig. 4c and Extended Data Fig. 8c). The $L1_0$ grain embedded in two large $L1_2$ phases exhibits an fcc lattice rather than the face-centred tetragonal lattice of bulk $L1_0$ FePt with a c/a ratio of 0.96. Together, these results confirm that the local chemical order rather than lattice distortion is the main source of MAE. Because there is no perfect $L1_0$ phase in the nanoparticle, the largest local MAE in the region (0.95 meV per atom) is smaller than that of an ideal $L1_0$ phase (1.40 meV per atom). The smallest MAEs exist in the $L1_2$ grain, and some sharp transitions from large to small MAEs are also observed. Figure 4d and Extended Data Fig. 8d show the local MAE distribution at an $L1_0$ and $L1_2$ grain boundary, overlaid with measured atomic positions and species. The sharp grain boundary is responsible for a sudden transition of the local MAE, suggesting that the MAE is highly localized.

Our DFT calculations using the measured atomic coordinates and chemical species also yield the spin and orbital magnetic moments. Extended Data Fig. 9a–d shows the histograms of the spin and orbital magnetic moments of the Fe and Pt atoms in the largest $L1_0$ grain. The average orbital magnetic moment of the Fe atoms is 0.08 ± 0.01 Bohr magnetons (μ_B), and the average spin and orbital magnetic moments of the Pt atoms are 0.31 ± 0.05 and 0.05 ± 0.01 μ_B, respectively, which are consistent with those reported elsewhere[24]. However, the average spin magnetic moment of the Fe atoms is 3.14 ± 0.06 μ_B, slightly larger than that of ideal $L1_0$ FePt (ref. 24). This enhancement is attributed to two factors: (i) the $L1_0$ grain is confined between two large $L1_2$ grains and has lower Fe coordination numbers, which enhances local magnetic moments (Extended Data Fig. 9e); and (ii) the $L1_0$ grain shares the fcc lattice parameters of the $L1_2$ grains. The expanded lattice constant along the c axis leads to enhancement of Fe spin magnetic moment owing to the magneto-volume effect[32]. Both the enhanced spin magnetic moments and their distributions signify the importance of correlating structure and properties at the single-atom level.

With the exponential growth of computing power and improvements in *ab initio* techniques, our measured atomic coordinates of the whole FePt nanoparticle with 23,196 atoms could be used as direct input for first-principles calculations. The local MAE and atomic magnetic moments extracted from the nanoparticle could then be used as parameters for micromagnetic simulations[33], whose precision is at present limited by parameters taken from either bulk or modelled values. Looking forward, the ability to determine the chemical order/disorder and crystal defects with high precision and to correlate their 3D atomic arrangements with material properties at the single-atom level is expected to find applications in materials science, physics, chemistry, nanoscience and nanotechnology.

Online Content Methods, along with any additional Extended Data display items and Source Data, are available in the online version of the paper; references unique to these sections appear only in the online paper.

Received 20 June; accepted 25 November 2016.

1. Miao, J., Ercius, P. & Billinge, J. L. Atomic electron tomography: 3D structures without crystals. *Science* **353,** aaf2157 (2016).
2. Bacon, D. J. & Hull, D. (eds) *Introduction to Dislocations* 5th edn (Butterworth-Heinemann, 2011).
3. Kelly, A. A. & Knowles, K. M. *Crystallography and Crystal Defects* 2nd edn (John Wiley & Sons, 2012).
4. Kelly, T. F. & Miller, M. K. Atom probe tomography. *Rev. Sci. Instrum.* **78,** 031101 (2007).
5. Midgley, P. A. & Dunin-Borkowski, R. E. Electron tomography and holography in materials science. *Nat. Mater.* **8,** 271–280 (2009).
6. Muller, D. A. Structure and bonding at the atomic scale by scanning transmission electron microscopy. *Nat. Mater.* **8,** 263–270 (2009).
7. Krivanek, O. L. *et al.* Atom-by-atom structural and chemical analysis by annular dark-field electron microscopy. *Nature* **464,** 571–574 (2010).
8. Pennycook, S. J. & Nellist, P. D. *Scanning Transmission Electron Microscopy: Imaging and Analysis* (Springer Science & Business Media, 2011).
9. Van Aert, S., Batenburg, K. J., Rossell, M. D., Erni, R. & Van Tendeloo, G. Three-dimensional atomic imaging of crystalline nanoparticles. *Nature* **470,** 374–377 (2011).
10. Bals, S. *et al.* Three-dimensional atomic imaging of colloidal core-shell nanocrystals. *Nano Lett.* **11,** 3420–3424 (2011).
11. Scott, M. C. *et al.* Electron tomography at 2.4-ångström resolution. *Nature* **483,** 444–447 (2012).
12. Chen, C.-C. *et al.* Three-dimensional imaging of dislocations in a nanoparticle at atomic resolution. *Nature* **496,** 74–77 (2013).
13. Goris, B. *et al.* Three-dimensional elemental mapping at the atomic scale in bimetallic nanocrystals. *Nano Lett.* **13,** 4236–4241 (2013).
14. Yang, H. *et al.* Imaging screw dislocations at atomic resolution by aberration-corrected electron optical sectioning. *Nat. Commun.* **6,** 7266 (2015).

15. Park, J. *et al.* 3D structure of individual nanocrystals in solution by electron microscopy. *Science* **349,** 290–295 (2015).
16. Xu, R. *et al.* Three-dimensional coordinates of individual atoms in materials revealed by electron tomography. *Nat. Mater.* **14,** 1099–1103 (2015).
17. Goris, B. *et al.* Measuring lattice strain in three dimensions through electron microscopy. *Nano Lett.* **15,** 6996–7001 (2015).
18. Haberfehlner, G. *et al.* Formation of bimetallic clusters in superfluid helium nanodroplets analysed by atomic resolution electron tomography. *Nat. Commun.* **6,** 8779 (2015).
19. Parr, R. G. & Yang, W. *Density-Functional Theory of Atoms and Molecules* (Oxford Univ. Press, 1994).
20. Jones, R. O. Density functional theory: its origins, rise to prominence, and future. *Rev. Mod. Phys.* **87,** 897–923 (2015).
21. Cullity, B. D. & Graham, C. D. *Introduction to Magnetic Materials* 2nd edn (Wiley, 2008).
22. Ju, G. *et al.* High density heat assisted magnetic recording media and advanced characterization — progress and challenges. *IEEE Trans. Magn.* **51,** 3201709 (2015).
23. Albrecht, T. R. *et al.* Bit-patterned magnetic recording: theory, media fabrication, and recording performance. *IEEE Trans. Magn.* **51,** 0800342 (2015).
24. Antoniak, C. *et al.* A guideline for atomistic design and understanding of ultrahard nanomagnets. *Nat. Commun.* **2,** 528 (2011).
25. Sun, S., Murray, C. B., Weller, D., Folks, L. & Moser, A. Monodisperse FePt nanoparticles and ferromagnetic FePt nanocrystal superlattices. *Science* **287,** 1989–1992 (2000).
26. Gruner, M. E., Rollmann, G., Entel, P. & Farle, M. Multiply twinned morphologies of FePt and CoPt nanoparticles. *Phys. Rev. Lett.* **100,** 087203 (2008).
27. Gruner, M. E. & Entel, P. Competition between ordering, twinning, and segregation in binary magnetic 3d-5d nanoparticles: a supercomputing perspective. *Int. J. Quantum Chem.* **112,** 277–288 (2012).
28. Antoniak, C. *et al.* Enhanced orbital magnetism in $Fe_{50}Pt_{50}$ nanoparticles. *Phys. Rev. Lett.* **97,** 117201 (2006).
29. Dmitrieva, O. *et al.* Magnetic moment of Fe in oxide-free FePt nanoparticles. *Phys. Rev. B* **76,** 064414 (2007).
30. Saita, S. & Maenosono, S. Formation mechanism of FePt nanoparticles synthesized via pyrolysis of iron(III) ethoxide and platinum(II) acetylacetonate. *Chem. Mater.* **17,** 6624–6634 (2005).
31. Ratke, L. & Voorhees, P. W. *Growth and Coarsening: Ostwald Ripening in Material Processing* (Springer Science & Business Media, 2002).
32. Krauss, U. & Krey, U. Local magneto-volume effect in amorphous iron. *J. Magn. Magn. Mater.* **98,** L1–L6 (1991).
33. Fidler, J. & Schrefl, T. Micromagnetic modelling — the current state of the art. *J. Phys. D* **33,** R135–R156 (2000).

Supplementary Information is available in the online version of the paper.

Acknowledgements We thank J. Shan, J. A. Rodriguez, M. Gallagher-Jones and J. Ma for help with this project. This work was primarily supported by the Office of Basic Energy Sciences of the US DOE (DE-SC0010378). This work was also supported by the Division of Materials Research of the US NSF (DMR-1548924 and DMR-1437263) and DARPA (DARPA-BAA-12-63). The chemical ordering analysis and ADF-STEM imaging with TEAM I were performed at the Molecular Foundry, Lawrence Berkeley National Laboratory, which is supported by the Office of Science, Office of Basic Energy Sciences of the US DOE (DE-AC02-05CH11231). M.E. (DFT calculations) was supported by the US DOE, Office of Science, Basic Energy Sciences, Material Sciences and Engineering Division. DFT calculations by P.K. were conducted at the Center for Nanophase Materials Sciences, which is a DOE Office of Science User Facility. This research used resources of the Oak Ridge Leadership Computing Facility, which is supported by the Office of Science of the US DOE (DE-AC05-00OR22725).

Author Contributions J.M. directed the project; F.S. and H.Z. prepared the samples; M.C.S., W.T., P.E. and J.M. discussed and/or acquired the data; Y.Y., C.-C.C., R.X., A.P.J., L.W., J.Z. and J.M. conducted the image reconstruction and atom tracing; C.O., Y.Y., H.Z., P.E., W.T., R.F.S., M.C.S. and J.M. analysed and interpreted the results; M.E., P.R.C.K., R.F.S., Y.Y., H.Z., C.O., W.T. and J.M. discussed and performed the DFT calculations; J.M., Y.Y., H.Z., P.E., C.O., W.T., M.E., P.R.C.K., R.F.S. wrote the manuscript.

Author Information Reprints and permissions information is available at www.nature.com/reprints. The authors declare no competing financial interests. Readers are welcome to comment on the online version of the paper. Correspondence and requests for materials should be addressed to J.M. (miao@physics.ucla.edu).

Reviewer Information *Nature* thanks M. Farle and A. Kirkland for their contribution to the peer review of this work.

METHODS

Sample preparation. FePt nanoparticles were synthesized following procedures published elsewhere[34]. Briefly, 0.5 mmol platinum(II) acetylacetonate ($Pt(acac)_2$) was mixed with 20 ml phenyl ether under a gentle flow of nitrogen (N_2). The mixture was heated to 120 °C, and kept at that temperature for 10 min with magnetic stirring. Under a nitrogen blanket, 1 mmol iron pentacarbonyl ($Fe(CO)_5$) was quickly injected, followed by sequential addition of 15 mmol oleic acid and oleylamine. The solution was heated to 220 °C in 20 min and kept at that temperature for one hour. Then the mixture was further heated to 260 °C and refluxed for another hour. After the solution was cooled down to room temperature, the nanoparticles were precipitated and purified by centrifugation. The collected nanoparticles were dispersed in hexane for storage.

Data acquisition. Samples were prepared by depositing a solution of the FePt nanoparticles in ethanol onto a 5-nm-thick silicon nitride membrane using an atomizer. After the particles were applied to the silicon nitride membrane, they were annealed at 600 °C for 25 min in high vacuum. A thin, ultra-pure carbon layer was then applied over the course of 5 min at 700 °C to enhance the conductivity of the membranes and to protect the particles from damage under the electron beam. Several tomographic tilt series were acquired from FePt nanoparticles using the TEAM I microscope and TEAM stage[35] at the National Center for Electron Microscopy in the Molecular Foundry. Images were acquired at 300 kV in ADF-STEM mode with a 30-mrad convergence semi-angle (resulting in a probe size of ~0.5 Å), 48 mrad and 251 mrad detector inner and outer semi-angles, and a beam current of 50–55 pA (Extended Data Table 1). A high-quality tilt series was selected for this study because of its rich structural variety (Extended Data Fig. 1). This tilt series was collected at 68 angles with a tilt range of −65.6° to +64.0°. Ten images per tilt angle were measured with 3 μs dwell time to minimize image blurring. Owing to imperfections in the calibration of the *x*- and *y*- scanning coils in the microscope's STEM scanning system, an additional correction was applied to the images to ensure square pixels. This scan distortion was measured using a standard sample under the same imaging conditions, and corrected using Fourier methods[36].

Sample size. No statistical methods were used to predetermine sample size.

Image de-noising. The 10 acquired images for each tilt angle were aligned by cross-correlation with 0.1 pixel steps and averaged. The ADF-STEM images collected with the TEAM I microscope exhibit Poisson-Gaussian mixed noise[16], and follow the noise model of $Y = \alpha P(n_e) + N(\mu_b, \sigma_b)$, where Y is the measured counts of each pixel, α is the gain parameter (counts per electron), $P(n_e)$ is the Poisson distribution of n_e electrons, and $N(\mu_b, \sigma_b)$ is the normal distribution of the mean μ_b and the standard deviation σ_b. The noise parameters α, μ_b, σ_b were estimated from the local mean and the variance based on spatial averaging of acquired images. The images were de-noised by sparse 3D transform-domain collaborative filtering[37], while Anscombe variance-stabilizing transformation and its inverse were applied to the images before and after de-noising with estimated noise parameters[38]. The robustness of this de-noising method has been tested by other experimental data sets and multislice simulations[16].

GENFIRE reconstruction. After de-noising, the 68 images were projected onto the tilt axis (*y* axis) to obtain 1D curves, and the images were aligned along the tilt axis by using cross-correlation among the 1D curves. During this process, the optimal background of each image was determined by maximizing the cross-correlation among the 1D curves and was subsequently subtracted from each image. Alignment along the *x* axis was achieved by the centre of mass method (ref. 11).

From the aligned tilt series, a 3D reconstruction was performed using GENFIRE. GENFIRE started with assembling a rectangular 3D Fourier grid from the measured images. For each image, its Fourier transform represents a plane slicing through the origin of the 3D Fourier grid (that is, the Fourier slice theorem[39]). For any Fourier grid point (k_x, k_y, k_z), a perpendicular distance (D_j) to the *j*th Fourier plane and the foot of the perpendicular line, (u_j, v_j), were calculated with $j = 1, 2, \ldots 68$. The value of (u_j, v_j) was computed from the *j*th image using the discrete Fourier transform instead of the fast Fourier transform (FFT) as (u_j, v_j) are non-integer coordinates. By repeating the above procedure, we calculated the values of all the (u_j, v_j) points with D_j smaller than a predefined threshold D_{th}, from which the value of the grid point, $F(k_x, k_y, k_z)$, was computed

$$F(k_x,k_y,k_z) = \sum_{\{j|D_j<D_{th}\}} \frac{D_j^{-1}}{\sum_{\{j|D_j<D_{th}\}} D_j^{-1}} \sum_{x=-\frac{N}{2}}^{\frac{N}{2}-1} \sum_{y=-\frac{N}{2}}^{\frac{N}{2}-1} f_{obs}^{j}(x,y) e^{\frac{-2\pi i(xu_j+yv_j)}{NO}} \quad (1)$$

where $f_{obs}^{j}(x,y)$ represents the *j*th measured image with a size of $N \times N$ pixels ($N = 256$ in this experiment) and O is the oversampling ratio[40,41]. By properly choosing the oversampling ratio and the predefined threshold ($D_{th} = 0.05$ voxels and $O = 4$ in this case), we accurately computed the values of a small fraction of grid points from the images using equation (1). For the remaining grid points without any (u_j, v_j) point satisfying $D_j < D_{th}$, we set them as undefined. The algorithm then iterated between real and reciprocal space using the FFT and its inverse. In real space, a support and positivity were incorporated as constraints. In this case, a $256 \times 256 \times 256$ voxel cube with smoothed edges was used as a support. In each iteration, the values outside the support and the negative values inside the support were set to zero. In reciprocal space, the grid points with measured data were enforced as constraints in each iteration, while the values of the undefined grid points were iteratively updated by the algorithm. The algorithm was monitored by an error metric in each iteration, defined as the difference between the values of the measured and calculated grid points. After 500 iterations, the error metric could not be further improved and an initial 3D reconstruction was obtained.

To identify atomic positions and species with high precision, we have implemented a method to refine the tilt angles from the initial 3D reconstruction, which is routinely used in single-particle cryo-electron microscopy[42,43]. For each tilt orientation, we found the corresponding three Euler angles (φ, θ, ψ) and scanned each of the Euler angles with a small angular increment. At each increment, the 3D reconstruction was projected back to calculate a 2D image. An error metric, defined as the difference between the calculated and measured images, was computed. By scanning all the three angles, we obtained an optimal set of the Euler angles for the tilt orientation, corresponding to the minimum error metric. This procedure was repeated for all the tilt orientations (angles). In this experiment, since θ was very small, the φ and ψ axes were almost collinear with each other. Thus, we fixed ψ and only scanned θ and φ for angular refinement. Because it is computationally intensive to calculate 2D images from a 3D reconstruction, we refined θ and φ sequentially. We first scanned θ and used GENFIRE with the refined θ angles to compute a new 3D reconstruction. We then repeated this procedure for the φ angles. The angular refinement and reconstruction procedure were iterated until there was no further improvement, producing a final 3D reconstruction. Our numerical simulation and additional experimental results have indicated that GENFIRE produces superior 3D reconstruction relative to other iterative tomographic methods[44,45]. These results will be presented elsewhere.

3D identification of atomic coordinates and chemical species. The 3D atomic positions and species of the FePt nanoparticle were determined using the following procedure.

(I) All local intensity maxima were identified from the final 3D reconstruction. Starting from the highest intensity peak, a 3D Gaussian function of $5 \times 5 \times 5$ voxels was fitted to the peak[16]. If this peak was satisfied with a minimum distance constraint (that is, the distance between two neighbouring atoms was ≥ 2 Å), it was added to a peak position list. This minimum distance constraint is justified as the covalent diameter of an Fe atom is 2.52 Å. Repeating this step for all the local intensity maxima resulted in 28,800 peaks. These peaks were also manually checked to ensure there were no misidentifications. During this process, 446 peaks in the list were adjusted and 525 new peaks were added by using manual Gaussian fitting of some local intensity maxima, producing a total of 29,325 peaks.

(II) Extended Data Fig. 2a shows a histogram of the identified peaks. Each peak should belong to one of the three categories: potential Pt atoms, potential Fe atoms and potential non-atoms. To separate these peaks, we developed an unbiased atom classification method using the following steps. (a) We selected a small fraction (0.6%) of peaks with the lowest intensity and obtained an average non-atom distribution ($5 \times 5 \times 5$ voxels) from them. We then chose an initial threshold between the Pt and Fe peaks. For all the remaining peaks, those larger or smaller than the threshold were used to calculate an average Pt or Fe atom, respectively, each with a size of $5 \times 5 \times 5$ voxels. (b) For each identified peak, three error functions were calculated,

$$E_{Pt} = \sum_i |P_i - A_i^{Pt}| \qquad E_{Fe} = \sum_i |P_i - A_i^{Fe}| \qquad E_{NA} = \sum_i |P_i - A_i^{NA}| \quad (2)$$

where P_i is the *i*th voxel intensity of the peak, A_i^{Pt}, A_i^{Fe} and A_i^{NA} are the *i*th voxel intensity of the averaged Pt, Fe and non-atom, respectively. Using equation (2), all the peaks were re-classified into three categories based on the minimal error function. (c) From the updated three categories, we re-calculated the average Pt and Fe atoms. Based on the updated average Pt and Fe atoms, we used equation (2) to classify all the peaks again to produce another three categories. This step was repeated until there was no change of the belonging of each peak to one of the categories, resulting in 13,917 Pt and 9,519 Fe atom candidates and 5,889 non-atoms (Extended Data Fig. 2b–d). This method is unbiased as we obtained very consistent results using a different fraction number from 0.6% and a different initial threshold value between the Pt and Fe peaks.

(III) Carefully examining the 5,889 non-atom peaks identified from step (II) suggested that some potential atoms might be incorrectly classified into this category. To mitigate this problem, we implemented a less aggressive method to re-classify the non-atom category. For every peak identified in step (I), we quantitatively compared it to an average Fe atom obtained from step (II) and a constant background. If it matched more with the average atom, it was selected as an atom

candidate. Otherwise, it was classified as a non-atom. Repeating this step for all 29,325 peaks with some minimal manual intervention produced 23,804 atom candidates and 5,521 non-atoms. Using the unbiased atom classification method (step II)), we classified 23,804 atom candidates into 14,216 Pt and 9,588 Fe atom candidates (Extended Data Fig. 2e–g).

(IV) Next, we quantified the peak intensity of the atoms in the missing wedge direction and found the average atom intensity is lower than that in the other regions. To mitigate this problem, we selected 5,445 atom candidates in the missing wedge region and applied the unbiased atom classification method (step II)) to separate these atoms. Collectively, steps (I)–(IV) produced 17,087 Pt and 6,717 Fe atom candidates.

(V) To validate the robustness of our method with regard to the choice of the minimum distance, we repeated steps (I)–(IV) using a minimum distance of 1.6 Å and obtained 16,551 Pt and 6,639 Fe atom candidates. The two different atomic models with a minimum distance of 1.6 Å and 2.0 Å were quantitatively compared, resulting in 23,145 common pairs and 659 non-common atoms. Among the 23,145 common pairs, 22,304 pairs were identified as the same species and 841 atom candidates were opposite species. To examine these non-common atoms and opposite atomic species, we used the 68 measured images with the following procedure. (1) Each of the measured images was converted to a Fourier slice by the FFT. (2) 68 Fourier slices were calculated from an atomic model by

$$F^{j}_{\mathrm{calc}}(\boldsymbol{q}) = \sum_{n=1}^{N} H_{A_n} f_{\mathrm{e}}(q) \mathrm{e}^{\frac{-B'_{A_n} q^2}{4} - 2\pi i \boldsymbol{r}_n \cdot \boldsymbol{q}} \tag{3}$$

where N is the number of atoms, $A_n = 1$ if the nth atom is Fe, $A_n = 2$ if the nth atom is Pt, H_1 and H_2 are the scaling factors for Fe and Pt atoms, respectively, $f_e(q)$ is a normalized electron scattering factor, $\boldsymbol{r}_n$ is the position of the nth atom, and B'_1 and B'_2 account for the electron probe size (50 pm), the thermal motions, and the reconstruction error of the Fe and Pt atoms, respectively. (3) An error function between the measured, $F^{j}_{\mathrm{obs}}(\mathbf{q})$, and calculated Fourier slices were computed:

$$E = \sum_{j,q} \left| F^{j}_{\mathrm{calc}}(\boldsymbol{q}) - F^{j}_{\mathrm{obs}}(\boldsymbol{q}) \right|^2 \tag{4}$$

(4) The 659 uncommon atom candidates were sorted from the highest to lowest intensity. Using the 23,145 common atoms as an initial model, the uncommon atoms, starting from the highest intensity, were cumulatively added one by one as Fe atom candidates to produce different models. For each model, the error function E was minimized by adjusting H_1, H_2, B'_1, and B'_2. By selecting the minimum error from all the models, we identified 37 uncommon atoms as real atoms. (5) For the 841 atom candidates with opposite species, we used the similar procedure described in previous steps to confirm that 240 are Pt atoms and 601 are Fe atoms.

(VI) Based on the atomic coordinates and species identified through steps (I)–(V), we examined every atom and manually adjusted 37 atoms, producing a 3D model of 23,196 atoms with 6,569 Fe and 16,627 Pt atoms. Note that manual adjustment of a very small fraction of atoms is routinely used during the atom tracing and refinement process in protein crystallography[46].

(VII) The 3D atomic model was refined[16] and then linearly projected back to calculate 68 images at the experimental angles. An R_1 factor was computed between the jth measured, $f^{j}_{\mathrm{obs}}(x, y)$, and calculated, $f^{j}_{\mathrm{calc}}(x, y)$, images,

$$R_1 = \frac{\Sigma_{x,y} \left| f^{j}_{\mathrm{obs}}(x, y) - f^{j}_{\mathrm{calc}}(x, y) \right|}{\Sigma_{x,y} \left| f^{j}_{\mathrm{obs}}(x, y) \right|} \tag{5}$$

The average R_1 for 68 pairs of images was 9.6%.

Multislice STEM simulations. A tilt series of 68 images with refined experimental Euler angles were calculated using multislice simulations[47]. A total of 68 cubic super cells with $a = 100$ Å were created. The final 3D atomic model was placed within the super cells. Individual super cells were divided into multiple 2.0-Å-thick slices along the z-axis, with 1,800 × 1,800 pixels sampling in the x and y axes for both the specimen and probe. The experimental parameters (300 keV electron energy, 0 mm C_3 aberration, 5 mm C_5 aberration, 30 mrad convergence semi-angle, 48 and 251 mrad detector inner and outer semi-angles) were used for the simulations, resulting in a tilt series of ADF-STEM images with 255 × 255 pixels per image and a pixel size of 0.37 Å. For each tilt angle, 16 frozen phonon configurations were simulated and averaged to obtain a calculated image. Each multislice image was convolved with a Gaussian function, whose width was determined by minimizing the error between the measured and simulated images. This procedure was used to account for the electron probe size and other incoherent effects. Extended Data Fig. 4 compares the measured and multislice simulated images at 0° tilt. A 3D volume was then reconstructed from the simulated tilt series with GENFIRE, and a new 3D model was obtained by using the same atom tracing procedure. A total of 23,324 atoms were traced, comprising 16,577 Pt and 6,747 Fe atoms. 23,043 common pairs of the atoms between experimental and multislice 3D model were selected based on the criterion that each pair should be within the radius of the Fe atom. Among the common pairs, 6,401 common pairs were identified as Fe atoms (97.4%), and 16,562 common pairs were identified as Pt atoms (99.6%), resulting in 99.0% of all atoms having been correctly identified. A histogram of the atomic deviation between the common pairs is shown in Extended Data Fig. 4d, indicating a root-mean-square deviation of 22.2 pm.

Determining the SROP of all phases present in the FePt nanoparticle. We used the atomic positions and species to classify the chemical order/disorder of the nanoparticle. This was done with the SROP of all possible phases present[48,49]. SROPs are typically over a shell of equivalent neighbouring atomic sites, and scale linearly with the number of sites that are correctly occupied for a given phase. Normalization parameters were used to set the SROP equal to one for a perfectly ordered phase, and zero for a disordered phase with completely random chemical occupancies. Our analysis procedure was to calculate a weighted SROP, defined as a 3D-Gaussian sum using cross-validation to determine the standard deviation[50], over a given length scale for each phase. Then, each atomic site was assigned to the phase with the highest SROP. The FePt nanoparticle was therefore divided up into grains of different phases, with a measurement of the SROP at all atomic sites. In this study, we considered 16 possible ordered phases from the fcc lattice in the 3D FePt reconstruction: $FePt_3$ $L1_2$ (4), Fe_3Pt $L1_2$ (4), FePt $L1_0$ (6), Pt-rich A1 (1), and Fe-rich A1 (1), where the number in the parentheses represents the possible phase orientations. Atomic sites with a SROP below a threshold, determined with cross-validation[50], were initially assigned to disordered boundaries. After the initial grain location determinations, these disordered sites were then assigned to neighbouring grains according to their highest SROP values. This step was carried out to prevent disordered regions in thin 'pancake' regions between grains or at the nanoparticle surface from being classified as grains due to small SROP fluctuations.

DFT calculations. We used experimentally determined atomic coordinates and species as direct input for DFT calculations of magnetic properties. We implemented the local spin-density approximation of the exchange-correlation functional[51,52] to calculate the MAEs using two independent approaches.

First, we cut out a 1,470-atom supercell from a grain boundary between two large $L1_2$ grains, where the largest $L1_0$ grain is located. We then slid a 32-atom volume (2 × 2 × 2 unit cells) inside the supercell with a half-unit-cell per step along each direction and produced 1,452 32-atom volumes. The electronic structure calculations of these 32-atom volumes were performed using projector augmented-wave method[53] within the Vienna *ab-initio* simulation package (VASP)[52]. We used a plane-wave energy cut-off of 300 eV and applied periodic boundary conditions. The integration over Brillouin zones was performed using 6 × 6 × 6 k-point sampling and the spin–orbit coupling was included in the calculations. Because the easy axis and hard axis of the nanoparticle were not known *a priori*, we calculated the energies along three high symmetry axes ([001], [010] and [100]) of the underlying cubic structure. In a system with substitutional and topological defects, the easy axis can be locally distributed. Furthermore, the local symmetry may cause the system to develop biaxial anisotropy. Because we observed mainly $L1_0$ and $L1_2$ phases with substitutional defects, the uniaxial anisotropy energy was computed as the energy difference between the [100] and [001] directions as well as between the [010] and [001] directions.

Second, we validated the sliding local volume calculation by using a different approach. We cropped six nested supercells from the same region, containing 32 (2 × 2 × 2 unit cells), 108 (3 × 3 × 3 unit cells), 256 (4 × 4 × 4 unit cells), 500 (5 × 5 × 5 unit cells), 864 (6 × 6 × 6 unit cells) and 1,372 atoms (7 × 7 × 7 unit cells). The MAEs of these six supercells were calculated using the real-space locally self-consistent multiple scattering (LSMS) code[54]. We performed fully relativistic calculations by solving the Dirac equation for all electrons in the sample[55] and constrained the magnetic moment directions along the [001], [010] and [100] axes[56]. The Dirac equation was solved by directly calculating the Green's functions of the scattered electrons inside the material in real space. To achieve scalability to large systems, for each atomic site in the calculation cell we considered scattering within a finite volume only (that is, a local-interaction zone). For all the calculations presented here, we chose this local-interaction zone as a sphere with a radius of 12.5 Bohr radii and an angular expansion cut-off of $L_{\max} = 3$. Using this approach, we calculated the MAEs of the six nested supercells, which are consistent with those obtained from the sliding local volume calculation (Fig. 4a and Extended Data Fig. 8a). These results validated our sliding local volume approach to calculate the 3D distribution of the local MAE. Meanwhile, we also calculated the magnetic moment associated with each atomic site in the six supercells using the fully relativistic LSMS method[54]. The self-consistent calculations of the magnetic moments used the same parameters as the MAE calculation, and we solved the Dirac equations with a constraint that the magnetic moments on all sites point along the [001] direction. We assigned the spin and orbital magnetic

moment to each atomic site by calculating the expectation value of the spin density operator and integrating the resulting magnetization density over the atomic sphere assigned to each site. Extended Data Fig. 9 shows the spin and orbital magnetic moments of the Fe and Pt atoms in the largest $L1_0$ grain.

Last, to estimate the influence of the uncertainty in the measured atomic coordinates, we selected four 32-atom, one 256-atom and one 500-atom volumes and relaxed their atomic positions with DFT. The structural relaxation was performed using the VASP with a $2 \times 2 \times 2$ k-point mesh[52]. The atomic positions were relaxed until forces were below 0.01 eV $Å^{-1}$. The root-mean-square deviation between the measured and relaxed atomic positions is 24.7 pm, which agrees with our precision estimation (22 pm). The MAEs of these six relaxed volumes were calculated by using the LSMS code[54]. The average MAE difference between the measured and relaxed volumes is 0.064 meV per atom.

Data availability. The experimental data, image reconstruction and data analysis source codes of the paper are freely available at www.physics.ucla.edu/research/imaging/FePt.

34. Xu, C. *et al.* FePt nanoparticles as an Fe reservoir for controlled Fe release and tumor inhibition. *J. Am. Chem. Soc.* **131,** 15346–15351 (2009).
35. Ercius, P., Boese, M., Duden, T. & Dahmen, U. Operation of TEAM I in a user environment at NCEM. *Microsc. Microanal.* **18,** 676–683 (2012).
36. Larkin, K. G., Oldfield, M. A. & Klemm, H. Fast Fourier method for the accurate rotation of sampled images. *Opt. Commun.* **139,** 99–106 (1997).
37. Dabov, K., Foi, A., Katkovnik, V. & Egiazarian, K. Image denoising by sparse 3-D transform-domain collaborative filtering. *IEEE Trans. Image Process.* **16,** 2080–2095 (2007).
38. Makitalo, M. & Foi, A. A closed-form approximation of the exact unbiased inverse of the Anscombe variance-stabilizing transformation. *IEEE Trans. Image Process.* **20,** 2697–2698 (2011).
39. Kak, A. C. & Slaney, M. *Principles of Computerized Tomographic Imaging* (SIAM, Philadelphia, 2001).
40. Miao, J., Sayre, D. & Chapman, H. N. Phase retrieval from the magnitude of the Fourier transforms of nonperiodic objects. *J. Opt. Soc. Am. A* **15,** 1662–1669 (1998).
41. Miao, J., Ishikawa, T., Robinson, I. K. & Murnane, M. M. Beyond crystallography: diffractive imaging using coherent X-ray light sources. *Science* **348,** 530–535 (2015).
42. Frank, J. *Electron Tomography: Methods for Three-Dimensional Visualization of Structures in the Cell* (Springer, 2010).
43. Gilbert, P. Iterative methods for the three-dimensional reconstruction of an object from projections. *J. Theor. Biol.* **36,** 105–117 (1972).
44. Miao, J., Förster, F. & Levi, O. Equally sloped tomography with oversampling reconstruction. *Phys. Rev. B* **72,** 052103 (2005).
45. Andersen, A. H. & Kak, A. C. Simultaneous algebraic reconstruction technique (SART): a superior implementation of the art algorithm. *Ultrason. Imaging* **6,** 81–94 (1984).
46. Brünger, A. T. *et al.* Crystallography & NMR System: a new software suite for macromolecular structure determination. *Acta Crystallogr. D***54,** 905–921 (1998).
47. Kirkland, E. J. *Advanced Computing in Electron Microscopy* 2nd edn (Springer Science & Business Media, 2010).
48. Finel, A., Mazauric, V. & Ducastelle, F. Theoretical study of antiphase boundaries in fcc alloys. *Phys. Rev. Lett.* **65,** 1016–1019 (1990).
49. Müller, M. & Albe, K. Lattice Monte Carlo simulations of FePt nanoparticles: influence of size, composition, and surface segregation on order-disorder phenomena. *Phys. Rev. B* **72,** 094203 (2005).
50. Kohavi, R. A study of cross-validation and bootstrap for accuracy estimation and model selection. In *Proc. 14th Int. Joint Conf. on A.I. Vol.* 2, 1137–1143 (Morgan Kaufmann, San Francisco, 1995).
51. Ceperley, D. M. & Alder, B. J. Ground state of the electron gas by a stochastic method. *Phys. Rev. Lett.* **45,** 566–569 (1980).
52. Kresse, G. & Joubert, D. From ultrasoft pseudopotentials to the projector augmented-wave method. *Phys. Rev. B* **59,** 1758–1775 (1999).
53. Blöchl, P. E. Projector augmented-wave method. *Phys. Rev. B* **50,** 17953–17979 (1994).
54. Wang, Y. *et al.* Order-*N* multiple scattering approach to electronic structure calculations. *Phys. Rev. Lett.* **75,** 2867–2870 (1995).
55. Eisenbach, M., Györffy, B. L., Stocks, G. M. & Újfalussy, B. Magnetic anisotropy of monoatomic iron chains embedded in copper. *Phys. Rev. B* **65,** 144424 (2002).
56. Stocks, G. *et al.* On calculating the magnetic state of nanostructures. *Prog. Mater. Sci.* **52,** 371–387 (2007).